

Accepted manuscript doi: 10.1680/jgeot.19.p.350

Accepted manuscript

As a service to our authors and readers, we are putting peer-reviewed accepted manuscripts (AM) online, in the Ahead of Print section of each journal web page, shortly after acceptance.

Disclaimer

The AM is yet to be copyedited and formatted in journal house style but can still be read and referenced by quoting its unique reference number, the digital object identifier (DOI). Once the AM has been typeset, an 'uncorrected proof' PDF will replace the 'accepted manuscript' PDF. These formatted articles may still be corrected by the authors. During the Production process, errors may be discovered which could affect the content, and all legal disclaimers that apply to the journal relate to these versions also.

Version of record

The final edited article will be published in PDF and HTML and will contain all author corrections and is considered the version of record. Authors wishing to reference an article published Ahead of Print should quote its DOI. When an issue becomes available, queuing Ahead of Print articles will move to that issue's Table of Contents. When the article is published in a journal issue, the full reference should be cited in addition to the DOI.

Saracho, A.C., Haigh, S.K. & Jorat, M.E. (2020) 'Flume study on the effects of microbial induced calcium carbonate precipitation (MICP) on the erosional behaviour of fine sand', *Geotechnique*. <https://doi.org/10.1680/jgeot.19.p.350>

Accepted manuscript doi: 10.1680/jgeot.19.p.350

Submitted: 22 November 2019

Published online in ‘accepted manuscript’ format: 03 July 2020

Manuscript title: Flume study on the effects of microbial induced calcium carbonate precipitation (MICP) on the erosional behaviour of fine sand

Authors: Alexandra Clarà Saracho*, Stuart K. Haigh* and M. Ehsan Jorat[†]

Affiliations: *University of Cambridge, Department of Engineering, Cambridge, UK and

[†]School of Applied Sciences, Abertay University, Dundee, UK

Corresponding author: Stuart K. Haigh, University of Cambridge, Department of Engineering, Cambridge, CB2 1PZ, UK.

E-mail: skh20@cam.ac.uk

Abstract

Tangential flow-induced interface erosion poses a major threat to a wide variety of engineering structures, such as earth-filled embankment dams, and oil- and gas-producing wells. This study explores the applicability of microbial induced calcium carbonate (CaCO_3) precipitation (MICP) via the ureolytic soil bacterium *Sporosarcina pasteurii* as a method for enhancing the surface erosion resistance of fine sand. Coarse-fine sand specimens were treated with cementation solution concentrations ranging between 0.02-0.1 M, and the erosional behaviour of the fine sand examined in a flume under surface-parallel flow and increasing shear stress. Photographs, cumulative height eroded-time series, and erosion rates were obtained as a function of specimen height, MICP treatment formulation, and CaCO_3 content. Results showed that while untreated specimens eroded primarily in particulate and mass form, MICP-treated specimens were characterised by a block erosion mechanism. Further, erodibility was found to depend on the amount of CaCO_3 precipitated and the concentration of the cementation solution used. To understand this, a systematic study of the CaCO_3 crystal sizes and distributions resulting from varying urea- CaCl_2 solution concentrations was undertaken through X-ray computed tomography. Fundamentally, the effectiveness of MICP for erosion control was found to be dominated both by the precipitated CaCO_3 content and microstructural features, with higher contents and larger crystals yielding lower erodibility values. It was also seen that crystal growth mechanisms could change depending on the urea- CaCl_2 solution concentration.

KEYWORDS: erosion; fabric/structure of soils; laboratory tests; reinforced soils; sands; shear strength

INTRODUCTION

Tangential flow-induced interface erosion poses a major threat to a wide variety of engineering structures, including earth-filled embankment dams, and oil- and gas-producing wells. This process occurs at the surface between soil and water or at the interface between two soil types (Regazzoni & Marot, 2013). The latter, termed contact erosion, generally starts along the interface between two different soils (*e.g.* coarse-fine soil interface), leading to the formation of a cavity. Surface erosion between the cavity walls and water is subsequently responsible for enlarging the pipe and may lead to rapid failure (Beguin, 2011; Bonelli, 2013; Murphy, 2018). In the context of zoned earth-embankment dams, the risk of interface erosion is located at the contact between the core and the foundation, and the core and the downstream filter (Philippe *et al.*, 2013). In hydrate-bearing reservoirs, such as the Daini-Atsumi Knoll Reservoir (where the first offshore methane production trial was conducted), it is the interface between the sandy hydrate-bearing layer and the overlying silt unit that is most likely to experience interface erosion (Murphy, 2018; Suzuki *et al.*, 2015; Yamamoto *et al.*, 2017).

Mechanical erosion control measures—*e.g.* downstream filters in earth-embankment dams and gravel packs in oil- and gas-producing wells—continue to be the most widely used approach in the dam and petroleum industries. Their overall philosophy is that of sand exclusion. This implies that while the detachment and transport of soil particles still occurs, these particles should not find an unfiltered exit point. Their proper functioning relies on the satisfaction of two contradictory requirements: a permeability criterion and a retention criterion (Terzaghi, 1922). On the one hand, the filter should be permeable enough to allow the passage of the fluid without local build-up of hydraulic gradient concentrations; and on the other, its openings should be small enough to prevent soil particle migration. This “geotechnical paradox”, together with the tendency for filters to become blocked, is prompting research and development into value-adding erosion control techniques. Moreover, to completely avoid the particle detachment by contact erosion, ICOLD (2016) recommends lowering the dam reservoir level, thus increasing the effective stress, decreasing permeability, and reducing seepage gradients; similarly, the conventional method in oil field development is to minimise the production rate (Mahmood *et al.*, 2018). These measures however, tend to be implemented as a result of emergency situations as they limit serviceability. It is clear therefore, that in these circumstances, a reactive risk management approach has been common practice in both industries.

Within this context, microbial induced calcium carbonate (CaCO₃) precipitation (MICP), a bio-mediated soil improvement technique that leads to the binding of soil grains by CaCO₃ crystals, has been gaining momentum (Amin *et al.*, 2017; Béguin *et al.*, 2019; Clara Saracho & Haigh, 2018a,b; Gao *et al.*, 2019; Haouzi *et al.*, 2020; Jiang & Soga, 2017; Jiang *et al.*, 2017, 2018, 2019; Salifu *et al.*, 2016; Wang *et al.*, 2018). More specifically, enzymatic hydrolysis of urea presents a relatively straightforward way to achieve MICP. This is because the urease enzyme is ubiquitous in microorganisms, yeast, and plants (Hammes *et al.*, 2003; Whiffin, 2004), and the growth of such organisms is easily induced using inexpensive chemicals. Ureolytic bacteria enzymatically hydrolyse urea (CO(NH₂)₂), resulting in the production of ammonium (NH₄⁺) and dissolved inorganic carbon (DIC), which in turn increase pH and favour CaCO₃ precipitation in the presence of soluble calcium ions (Equation 1):



The precipitated CaCO_3 results in a material that, aside from acting as a binding agent, retains the permeability of the soil matrix at low CaCO_3 contents (Al Qabany & Soga, 2013; Clarà Saracho & Haigh, 2018b; Whiffin *et al.*, 2007). However, its erosional behaviour is still not fully understood.

Critical shear stress and erosion rate are two of the measures commonly used in practice to quantify the sensitivity of fine-grained soils to surface erosion (Reddi *et al.*, 2000; Regazzoni & Marot, 2013). Historically, laboratory flumes have been employed to obtain direct measurements of the erosion function, *i.e.* erosion rate in terms of shear stress (Briaud *et al.*, 1999; Briaud *et al.*, 2001; Damgaard *et al.*, 1997; McNeil *et al.*, 1996; Ravens & Gschwend, 1999; Roberts *et al.*, 1998; White, 1970). Aside from previous studies performed by the authors (Clarà Saracho & Haigh, 2018a,b), there are only two other flume-based investigations available in the literature for MICP-treated sands (Amin *et al.*, 2017; Wang *et al.*, 2018). Wang *et al.* (2018) focused on surficial sand stabilisation using a polymer-modified MICP solution, which was applied once by surface percolation. This resulted in the formation of a surficials and crust, the erodibility of which was evaluated in an Erosion Function Apparatus (EFA) at shear stresses ranging from 39.2 to 1367 Pa, corresponding to a mean flow velocity of 1–6 ms^{-1} (after Briaud *et al.* 1999; Briaud *et al.* 2001). Wang *et al.* concluded that a 1 M CaCl_2 solution treatment is required for surface erosion and local bridge scour control. Amin *et al.* (2017) examined precipitated calcite homogeneity in relation to injection strategy using 0.5 and 0.75 M urea- CaCl_2 solutions. They also tested the different specimens in an EFA. A five-fold increase in critical shear stress values was obtained regardless of the injection strategy; and reductions in erosion rates were between 35-97%, with a double injection cycle of both bacteria and 0.5 M urea- CaCl_2 solutions yielding the largest, yet least uniform improvement. The reason why different treatment formulations yielded different erosion rates, with similar CaCO_3 contents, was, however, not discussed. The first caveat of both studies is the discrete nature of the erosion measurements acquired. Because the shape of the erosion-time series is expected to vary greatly as a function of CaCO_3 precipitation content and treatment formulation, a linear erosion law is insufficient to fully understand erosional patterns. For this, visual inspection and continuous monitoring of the eroding specimen are necessary. The second caveat is the fact that both studies still resort to the CaCO_3 content as the ultimate parameter defining the erosion behaviour of soils, despite existing evidence pointing towards a dependency between CaCO_3 microstructure and macromechanical response (Dadda *et al.*, 2019; Terzis & Laloui, 2018; Wang, 2018).

To this end, this study aimed to characterise the effect of different CaCO_3 crystal sizes and distributions—resulting from varying urea- CaCl_2 solution concentrations—on the surface erosion behaviour of fine sand. A series of erosion tests were conducted using a newly designed erosion flume system, which allowed the continuous acquisition of erosional data. To demonstrate its proper functioning, results for untreated specimens were compared with other studies of a similar nature. Next, by using surface erosion parameters *viz.*, critical shear stress, erosion rate, and erodibility (*e.g.* Briaud *et al.* 2001; Reddi *et al.* 2000; Roberts *et al.* 1998), a better understanding of how MICP might influence a surface erosion law for fine sand was obtained. Finally, the microstructural characteristics of the precipitated CaCO_3 crystals were quantified by X-ray computed tomography (CT) and visualised by scanning electron microscopy (SEM).

EXPERIMENTAL DETAILS

Erosion Function Apparatus (EFA) design

An Erosion Function Apparatus (EFA) was designed to measure the erosion of sand specimens at varying fluid flow-induced shear stresses (Figure 1). Similar setups have been described by Briaud *et al.* (2001); McNeil *et al.* (1996); Ravens Gschwend (1999); Roberts *et al.* (1998). The EFA is a 1 m long straight flume with width and height of 60 mm and 25 mm, respectively. The main components are the coring tube; the test section; an inlet section with a flow straightener to stimulate development of the bottom boundary layer; a flow exit section; a water storage tank; and a pump. In addition, a water delivery system is used to monitor the water flow rate and pressure delivered to the flume. This consists of a control valve, which provides control over the flow rate in the flume, and a flow meter, positioned between the pump and the valve.

At the start of each test, an actuator is used to drive the specimen through the circular opening in the bottom of the test section until it protrudes 1 mm from the bottom of the flume. Water is pumped through the flume at a specific flow rate, thus imposing a particular shear stress on the surface of the specimen and causing it to erode. A laser (beam diameter = 0.5–0.9 mm) reflecting on the centre of the soil surface in the flume is configured to continually move the actuator so that the soil-water interface remains at 1 mm above the bottom of the flume. The progress of erosion is thus recorded as the upward movement of the specimen in the coring tube by means of a LVDT.

The shear stress τ applied on the walls of the flume is established through the Darcy-Weisbach equation (after Briaud *et al.* 1999), relating τ with the cross-section averaged velocity v by means of a friction factor f :

$$\tau = \frac{1}{8} f \rho_w v^2 \quad (2)$$

where ρ_w is the density of water. The Moody chart (Moody, 1944), modified for flow through a rectangular pipe, provides f as a function of the flow regime, characterised by the pipe roughness ϵ and the Reynolds number Re :

- The pipe roughness after Nikuradse (1933):

$$\epsilon = k_s / D \quad (3)$$

where k_s is the grain-related roughness height taken equal to half the mean particle diameter $D_{50} / 2$ and D is the diameter of the pipe. Since the flume in the EFA has a rectangular cross-section, D is taken as the hydraulic diameter $D = 2ab / (a + b)$, where a and b are the dimensions of the sides of the rectangle.

- The liquid and the type of flow, characterised by the Reynolds number:

$$Re = vD / \nu \quad (4)$$

where ν is the kinematic viscosity of water ($10^{-6} \text{ m}^2 / \text{s}$).

Tests ran at sequentially higher shear stresses, ranging from 0.0007 to 0.17 Pa and corresponding to a mean velocity in the flume of 0.033–0.18 ms^{-1} . Eleven different shear stresses were tested, with each step lasting for 10 min. This enabled the determination of erosion rates at several different shear stresses and distances from the coarse-fine sand interface using only one core. This cycle was repeated until either all the fine sand was eroded from the core or erosion ceased.

Specimen preparation

As shown in Figure 2, Polytetrafluoroethylene (PTFE) cylindrical tubes were dry packed with a filter-soil layer consisting of 25 mm of Fraction A silica sand ($D_{50} = 1.61$ mm) overlying a base-soil layer consisting of 25 mm of Fraction D silica sand, with properties shown in Table 1. Sands were supplied uncrushed, dried, and washed by David Ball Specialist Sands (UK). Thus, they were free of organics, clay or silt. All specimens were prepared to the same target dry density by gently tapping their side with a tamping rod. This allowed the post-treatment comparison of CaCO_3 microstructural properties and resulting erosional behaviour.

The cores were oriented vertically with acrylic top and bottom caps, and a metallic filter mesh was placed adjacent to the bottom cap to prevent soil migration out of the cores. Additionally, bottom ports were fitted with tubing to allow full control of drainage conditions during MICP treatment.

MICP treatment

Sporosarcina pasteurii (strain designation ATCC 11859) was used to obtain the MICP-treated specimens. This was grown in petri dishes, prepared under sterile conditions in an ammonium-yeast extract (NH_4 -YE) medium (ATCC medium: 1376) and incubated at 30°C for 24–48 h. A single colony was subsequently resuspended in an agar-free NH_4 -YE liquid medium also prepared under sterile conditions. This bacterial solution was incubated at 30°C in a shaking incubator for 24 h (200 rpm) to an optical density (OD_{600}) of 1.5–2.0.

Following the injection from the top of the specimen by gravity of 2 pore volume (PV) of deionised (DI) water, 1 PV of the bacterial solution was injected in the same way. Bacteria were allowed a 24 h period to attach to the sand particles before introducing 1 PV of the cementation solution, also from the top of the core. This procedure of injection-retention of the cementation solution was repeated every 24 h for a 10-day period. The cementation liquid medium consisted of a premixed solution of urea ($\text{CO}(\text{NH}_2)_2$) and calcium chloride (CaCl_2) with a molar ratio of 3:2, in addition to 3g L^{-1} of Nutrient Broth and 10g L^{-1} of sodium bicarbonate (NaHCO_3), all dissolved in DI water. Table 2 summarises the compositions and the injection scheme adopted for this study.

It should be noted that specimens were treated with the coarse sand overlying the fine sand, and inverted for EFA testing (*cf.* Figures 1 and 2). This configuration was adopted to simulate field implementation. In zoned earth-embankment dams, MICP treatment would be applied from the permeable, coarse layers (*e.g.* downstream filter, foundation) into the more impervious, fine soil core, with the objective of targeting the contact between the two zones. Similarly, in oil- and gas-producing reservoirs, the injection direction would be from the extraction well, through the gravel pack, and into the formation. In both scenarios, it is the fine fraction which is the most susceptible to tangential-flow induced erosion, and thus it is the fine sand's erosional behaviour that investigated in the EFA. It is acknowledged however, that at field scale, erodibility is higher at the interface, where the velocity gradient induced by the permeability change between granular materials is greatest. The EFA tests were therefore carried out at a decreasing distance from the coarse-fine sand interface and results evaluated with respect to the CaCO_3 vertical profiles and XRCT volume reconstructions.

CaCO_3 measurement and visualisation

The vertical profile of the precipitated CaCO_3 inside the MICP-treated specimens was determined after treatment completion through inductively coupled plasma optical emission spectrometry (ICP-OES), set to detect calcium (Ca). Samples were prepared by dissolving 0.05 g of biocemented sand in 5 mL of 1 M hydrochloric (HCl) acid and soaked for 24 h. In

addition, to account for unreacted traces of calcium from the cementation solution, measurements of samples rinsed with 5 mL of DI water, also soaked for 24 h, were taken and subtracted as follows:

$$c[\text{Ca}^{2+}]_{\text{Final}} = c[\text{Ca}^{2+}]_{\text{HCl}} - c[\text{Ca}^{2+}]_{\text{DI}} \quad (5)$$

The CaCO_3 content was then calculated as:

$$\% \text{ of Ca in CaCO}_3 = \frac{M(\text{Ca})}{M(\text{CaCO}_3)} = 40.04\% \quad (6a)$$

$$\therefore \text{CaCO}_3 (\text{wt}\%) = \underbrace{\frac{c[\text{Ca}^{2+}]_{\text{Final}} \cdot V_{\text{SOLV}}}{\text{mg of Ca}^{2+}}}_{\text{mg of CaCO}_3} \cdot \frac{100}{40.04} \frac{1}{w_s} \quad (6b)$$

where $M(\text{Ca})$ and $M(\text{CaCO}_3)$ are the molar weights; $c[\text{Ca}^{2+}]$ is the analyte solution concentration measured by the ICP-OES; $V_{\text{SOLV}} = 5 \text{ mL}$ is the volume of solvent; and $w_s = 0.05 \text{ g}$ is the weight of the MICP-treated sand sample.

For each vertical location, ICP-OES measurements were performed in triplicate, with data presented as mean \pm standard deviation (SD). A 6-point calibration line was determined by preparing standard solutions with Ca^{2+} ion concentrations ranging between 1–150 mgL^{-1} , obtaining a coefficient of correlation of 0.999. The emitted photon intensities of the calibration standards were then back-calculated to compute the accuracy, data are presented in Table 3. Except for the 1.0 mgL^{-1} concentration, accuracy ranged from 98.6 to 106.1% and the precision as relative standard deviation (RSD) from 0.7 to 1.9%. The lower accuracy and precision obtained for the 1 mgL^{-1} standard had a negligible effect on the obtained results, as measured Ca^{2+} concentrations were typically $>10 \text{ mgL}^{-1}$ (Figure 3). In addition, precision as RSD ranged between $\pm 5\%$ for all measured samples, exponentially decreasing with increasing Ca^{2+} concentration and independent of vertical location (for the used Ca^{2+} concentration range).

The 3-dimensional pore space of the soil was visualised with an X-TEK HMX 225 microtomography system (Nikon Metrology, Tring, Herts, UK) at Abertay University. The entire volume was scanned at a resolution of 13 μm , with an energy of 85 kV, a current of 100 μA , 3010 angular projections, and a 0.5 mm aluminium filter to reduce beam hardening. VGStudio Max v. 3.2 was used to convert volumetric images into a 16-bit grayscale image stack.

For the XRCT, MICP was induced in cylindrical samples with a 13 mm diameter and 27 mm in height. The specimen preparation and treatment scheme was analogous to that described above. This diameter was used to provide the optimum scanning resolution for the analysis of the calcite volume fraction. To facilitate the identification of the CaCO_3 crystals within the scanned volume, a 9.83 mm^3 pure calcite crystal with a density of 2710 kg/m^3 was attached to the exterior of the cylindrical samples prior to the scanning procedure. Subsequently, the grey-scale histograms of the images stack at VGStudio Max were narrowed to only observe this pure calcite crystal. Smaller particles of the same substance were thus identified within the samples after histogram thresholding. Since the samples only consisted of two elements—*i.e.* silica and CaCO_3 —, the observed particles within the cylindrical samples were identified as precipitated calcite. The porosity analysis function of the software was then used to calculate microstructural properties—*i.e.* volume of the calcite particles, surface area,

diameter. The volume of the pure calcite crystal used for the identification was subsequently deducted from the calculated total volume of the calcite crystals in the cylindrical samples.

It should be emphasised that the XRCT resolution was not sufficient to capture precipitated calcite nano-crystals, generally associated with abiotic primary precipitation. Nonetheless, these are not expected to contribute to the bonding of sand particles in a substantial way and their presence is likely to be consistent across specimens. For the purposes of this study, it was more critical to establish relative differences in the microstructural fabric between specimens rather than to accurately determine the CaCO_3 volume fraction. Discussions of the general trends would not be altered by a more precise determination of the 3D crystal structure.

Finally, the XRCT results were validated with a Phenom Pro Generation 5 Desktop scanning electron microscope (SEM). First, crystal size data was qualitatively assessed using SEM images of CaCO_3 crystals obtained from the middle of the Fraction D sand (10–20 mm from the coarse-fine sand interface). Second, microstructural quantities for the Fraction D sand of specimen MICP-0.04 M were compared with parameters measured directly under the SEM microscope. For this, the magnification was set to $480\times$, allowing the inspection of 4-6 fine sand grains per image. All samples were uncoated and images were acquired under backscattered scanning electron microscopy mode (SEM BSE).

RESULTS AND DISCUSSION

Calcium carbonate content

Figure 4 shows the vertical profile of the CaCO_3 content across the five cores, with details of sampling locations. As expected, CaCO_3 content increased with the urea- CaCl_2 solution molarity. This was most evident in the coarse layer, where precipitated mass ranged from approximately 0.4 to 2 wt%, for the MICP-0.02 M and MICP-0.1 M specimens, respectively. Conversely, CaCO_3 contents in the fine fraction were significantly lower, ranging from 0.1 to 0.8 wt%. Results consistently showed that the coarse-fine sand interface was heavily cemented, with CaCO_3 contents approximately 2-times greater than in the bulk fine material (see zoomed in plot in Figure 4). This “preferential” cementation was consistent with the results presented in two previous studies by the authors, where coarse-fine sand specimens were treated with increasing number of injections of urea- CaCl_2 solution ($[\text{CaCl}_2]=0.25\text{M}$ and $[\text{urea}]:[\text{CaCl}_2]=3:2$) (Clarà Saracho & Haigh, 2018a,b), and may translate into a higher erosion resistance of that zone. This will be further examined with the surface erosion data from the EFA tests.

Because the concentration of Ca^{2+} ions remained constant for a given urea- CaCl_2 solution concentration, precipitated CaCO_3 differences within the same specimen are most likely attributed to a non-uniform distribution of bacteria. When the bacterial density is higher, more urea is hydrolysed into CO_3^{2-} , resulting in higher CaCO_3 contents. Because CaCO_3 contents were consistently 2-times greater in the coarse-fine sand interface than in the bulk fine material, higher bacterial densities would be expected in that region. To understand the underlying reason for this, it is necessary to examine how the MICP process adapts to the porous medium of a soil matrix. Substantial work in this direction was carried out by Wang (2018), who used a microfluidic chip to investigate micro-scale fundamentals of MICP. Wang observed that *S. pasteurii* cells aggregate following the injection of the urea- CaCl_2 solution and that aggregate sizes increase with bacterial density and solution concentration. With this in mind, the present results further suggest that bacterial cells formed larger aggregates in the overlying coarse sand due to the larger pore sizes. These bacterial

aggregates were subsequently trapped by the coarse-fine sand interface, leading to a “preferential” CaCO_3 cementation. The accumulation of organic by-products of bacterial activity and/or extracellular polymeric substances (EPS) that surround bacterial cells forming biofilms (Rodríguez-Navarro *et al.*, 2007) could have further contributed to this phenomenon. These observations echoed the hypothesis of Terzis & Laloui (2018) that bio-chemical and transport phenomena during MICP adapt differently to varying base materials’ initial pore space. In addition, because the size of bacterial aggregates increases with urea- CaCl_2 solution concentration (Wang, 2018), these can eventually clog the soil pores. This would explain why the CaCO_3 contents of MICP-0.1 M in the fine sand were smaller than those of MICP-0.08 M, while those in the coarse sand were greater. Further research is however required to correlate the pore size, bacterial and urea- CaCl_2 solution concentrations, and the resulting size of bacterial aggregates. A microfluidic chip would be a very suitable experimental device to optimise MICP treatment in this area.

The affinity for precipitating at the coarse-fine sand interface was also observed from the XRCT scans shown in Figure 5, where specimens MICP-0.02 M, MICP-0.06 M, and MICP-0.1 M are displayed as representative examples. From the 2D cross sections it is clear that the calcite crystals at the bottom (Section B-B) were very localised and constituted a small volume fraction. Conversely, larger surfaces and crystal numbers were precipitated in the vicinity of the coarse-fine sand interface (Section A-A). From the 3D reconstruction in Figure 5 it can also be observed that the volumes of calcite in the coarse sand were larger than those in the fine sand. This lent some support to the formation of bacterial aggregates that were retained in the coarse matrix and affected the vertical profile of precipitated CaCO_3 . Regarding the microstructural properties, clear differences were also observed between urea- CaCl_2 treatment concentrations in the fine sand, with crystal sizes and total volumes increasing with reactant concentrations. This happened at the expense of crystal size uniformity. The XRCT results for the fine sand will be further analysed later and their validity discussed.

Observations of erosion patterns

Erosion of untreated fine sand was measured and compared with that of MICP-treated samples. For the untreated specimen (Figure 6), a sustained surface particulate erosion was established when the flow-induced stresses exceeded a critical shear stress u_c of approximately 0.1 Pa (0.14 m s^{-1}). Nonetheless, a small, nonzero value for cumulative height eroded was already observed at the smallest flow rates applied, suggesting a range of threshold shear stresses. Indeed, as the shear stresses are increased, more particles participate in the process of erosion, transport, and deposition, and the movement becomes more sustained. Because this transition happens gradually, it is very difficult to precisely define the shear stress, τ_c , at which movement is triggered. For this reason, and after similar approaches adopted in the literature (McNeil *et al.*, 1996; Roberts *et al.*, 1998), τ_c was defined as the shear stress causing a rate of erosion E_c of 3.6 mm h^{-1} , 0.9 mm of erosion in 15min. The critical shear stress was thus calculated by linearly interpolating between erosion rates measured above and below 3.6 mm h^{-1} .

Calculated τ_c values for the untreated fine sand were then compared with two other flume studies. For shear stresses from 0.2 to 6.4 Pa , Roberts *et al.* (1998) determined the effects of particle size and bulk density ρ_d on the erosion of quartz particles, and found that for

particles larger than 222 μm , erosion rates are independent of ρ_d . They expressed their results in the form of

$$\begin{aligned}\tau_c &= \left(\frac{E_c}{A}\right)^{1/n} \rho_d^{-m/n} \quad \text{for } D_{50} < 222\mu\text{m} \\ \tau_c &= \left(\frac{E_c}{A}\right)^{1/n} \quad \text{for } D_{50} \geq 222\mu\text{m}\end{aligned}\tag{7}$$

where $E_c = 3.6 \text{ mmh}^{-1}$ and the constants A , n , and m depend on particle size ($5.7 \leq D_{50} \leq 1350 \mu\text{m}$). White (1970) determined τ_c for surficial beds of grains with diameters between 20–2000 μm . The results of both studies are plotted in Figure 7, together with those obtained from seven flume experiments reported here. Overall, they were in good agreement with Roberts *et al.* (1998) and were slightly below White (1970)—possibly due to small differences in density, unreported by White (1970), and the use of crushed plastic rather than natural sediment for the two tests with $D_{50} \approx 2000 \mu\text{m}$.

For $\tau > 0.16 \text{ Pa}$ (0.18 ms^{-1}) Figure 6 shows a change of erosion process from surface to mass erosion, with cumulative height eroded increasing step-wise with time. Indeed, τ_c is related to the drained shear strength of the sand and, at the surface, this only depends on the packing of the granular skeleton. However, as flow-induced stresses become large, the uplift forces caused by turbulent stresses induce (local) pore water under pressures, which cause lumps of sand to be pulled out (Briaud *et al.*, 2001; Winterwerp *et al.*, 2012). While distinguishing between surface and mass erosion is relevant to the free surface erosion model here, in contact erosion the occurrence (or not) of mass erosion will depend on soil layer interactions (*e.g.* cavity size and long-term stability). The transition between the various erosion modes for an untreated specimen is shown schematically in Figure 6, after boundaries proposed by Winterwerp *et al.* (2012).

Figure 8 shows the cumulative height eroded-time series for the MICP-treated specimens, which were measured as a function of flow rate (and hence τ) and specimen height. As described before, multiple tests were performed for every core, each consisting of eleven flow rates. Test labelling refers to the urea- CaCl_2 solution concentration and the distance from the coarse-fine sand interface. For example, MICP-0.02 M-25 mm refers to a core treated with 0.02 Molar of CaCl_2 , and with the EFA test starting at 25 mm from the coarse-fine sand interface. Variations in surface erosion values within one core may be attributed to varying CaCO_3 contents and microstructural features with specimen height. Confirmation of the latter however, requires further microstructural observations and is outside the scope of the present study.

Generally, cumulative height eroded decreased with an increase in the urea- CaCl_2 solution concentration. A major improvement was observed between specimens MICP-0.02 M (Figure 8a) and MICP-0.04 M (Figure 8b), with cumulative height eroded decreasing by one order of magnitude (from 20 to 3 mm). Furthermore, a third mode of erosion was observed, which became more prominent with increasing solution concentration: block erosion. This mode corresponded to the pulling out of strongly cemented blocks, and was consistent with Clarà Saracho & Haigh (2018a). At low solution concentrations (0.02 and 0.04 M), the detachment of blocks from the surface caused a new group of weaker inter-particle bonds to be exposed, leading to a new stage of surface and mass erosion. Conversely, at higher concentrations, every erosion step was accompanied with a partial relaxation of erosion and, although the detachment of blocks with a high CaCO_3 content still led to the exposure of weaker blocks,

erosion finally ceased for MICP-0.08 M (18 and 10 mm) (Figure 8d) and MICP-0.1 M (5 mm) (Figure 8e). This was attributed to the selective erosion of weakly cemented particles and/or blocks first, which progressively reinforced the mechanical resistance of the surface, leaving a very strong cemented matrix. The formation of these clusters of cemented sand particles was also reported by Jiang & Soga (2017) for MICP-treated sand-gravel mixtures, thought to reduce the likelihood of internal erosion. Note however, that the block erosion mechanism reported here is only relevant to flow-induced erosion across a free surface.

Visual inspection during and after EFA testing further revealed that block sizes increased with the concentration of the urea-CaCl₂ solution (Figure 9). Larger agglomerates of cemented sand particles were first observed for specimen MICP-0.04 M (15 and 10 mm) (Figure 9a). The size of these agglomerates hindered their transport and were thus eroded on both sides simultaneously, yielding higher erosion values than for MICP-0.04 M-25 mm. For concentrations above 0.04 M, failure happened parallel to the direction of the flow (Figure 9b), with the ultimate fracture always occurring in the coarse fraction (Figure 9c).

Erosion rates

Average erosion rates E were determined by dividing the cumulative height eroded by the time required to do so. Results for untreated Fraction D sand are shown in Figure 10. In all cases, E increased with τ , but the discrepancy between values was greatest for high shear stresses, with two tests yielding slightly higher erosion rate values. This was likely to be due to small flume movements during flow acceleration, leading to spurious erosion.

In addition, results were compared with three well-established empirical laws developed from flume-erosion studies with uniform steady surface-parallel flow. The simplest and most common expression is a linear erosion law written in the form (*e.g.* Ravens & Gschwend 1999; Walder 2016)

$$E = k_d (\tau - \tau_c) \quad \text{for } \tau > \tau_c \quad (8)$$

where k_d is generally referred to as the erodibility coefficient. Equation 8 can be made nonlinear by introducing an empirical exponent m ,

$$E = k_d^* (\tau - \tau_c)^m \quad \text{for } \tau > \tau_c \quad (9)$$

however, such an expression would make the units of k_d^* depend upon m .

Consequently, van Rijn (1984) defined a dimensionless erosion rate as

$$\Phi = \frac{G_d}{G_s} \frac{E}{\sqrt{(G_s - 1) g D_{50}}} \quad (10)$$

which, for loose sands ($130 \mu\text{m} \leq D_{50} \leq 1500 \mu\text{m}$), he empirically determined to be equal to

$$\Phi = 0.00033 D_*^{0.3} T^{1.5} \quad (11)$$

where $D_* = D_{50} [(G_s - 1) g / \nu^2]^{1/3}$ is a dimensionless measure of the mean grain size; $T = \tau / \tau_c - 1$ is the dimensionless measure of shear stress. The other variables introduced above are grain specific gravity $G_s = \rho_s / \rho_w$ and dry bulk specific gravity $G_d = \rho_d / \rho_w$, where ρ_w , ρ_s , and ρ_d are the bulk dry densities of water, grains, and sand, respectively; acceleration of gravity g ; and kinematic viscosity of water ν . It is noteworthy that Equation 10 implicitly includes the critical Shields parameter $\Theta_c = \tau_c / [(G_s - 1) g D_{50}]$, found in terms of $\Theta_c = f(D^*)$ and known as the Shields diagram (Figure 11, Shields 1936)-, it therefore constitutes yet another τ -based empiricism.

To get around this, Walder (2016) proposed to rewrite Equation 8 as

$$\Phi = \sqrt{\Theta_c} \Phi = \sqrt{\Theta_c} \frac{G_d}{G_s} \frac{E}{\sqrt{\tau_c / \rho_w}} \quad (12)$$

and sought a dimensionless equation using T and the sediment properties in the form of

$$\Phi = \alpha T^m \quad (13)$$

with α and m being determined by means of the log-transformed data of T and Φ . In this case, τ_c was calculated as $\tau(E_c = 3.6 \text{ mmh}^{-1})$. While this gave an average value of $\tau_c = 0.052 \text{ Pa}$, the Shields diagram indicated initiation of erosion at approximately $\tau_c = 0.16 \text{ Pa}$.

From Figure 10, it can be seen that all three erosion laws agreed reasonably well with the erosion rates obtained from the EFA, with the linear law (Equation 8) being the optimum fit ($R^2 = 0.81$ for $\tau > \tau_c$). Furthermore, although some erosion occurred at stresses below the calculated τ_c , the approach adopted herein, whereby $\tau_c = \tau(E_c = 3.6 \text{ mmh}^{-1})$, offered a more accurate value than the one predicted by the Shields diagram (Figure 11).

Moreover, MICP-treated specimens displayed an erosion relaxation behaviour, which would not be captured by a linear law. In this case, Figure 12 shows that the relationship between E and excess shear stress $\tau - \tau_c$ can be approximated as

$$E = C e^{k(\tau - \tau_c)} \quad (14)$$

where C and k depend on the specimen properties (*e.g.* density, CaCO_3 content). Because the excess shear stress range was rather small, Equation 14 and 9 gave essentially the same results. Generally, the slope of $E(\tau - \tau_c)$ in Figure 12 was steepest for the 0.02 M concentration and decreased as the treatment concentration increased. While all specimens displayed a constant gradient beyond τ_c , better fits were obtained at higher urea- CaCl_2 solution concentrations. Indeed, this was because at high concentrations, block erosion—characterised by a relaxation of E with time (Figure 8)—became the predominant mode of erosion.

From Equation 14, it is possible to calculate the erodibility κ_d as the rate of change of erosion rate E with respect to the excess shear stress $\tau - \tau_c$,

$$\kappa_d = \frac{\partial E}{\partial(\tau - \tau_c)} = C k e^{k(\tau - \tau_c)} \quad (15)$$

dependent upon the magnitude of the applied shear stress. Results in Figure 12 were therefore used to compute κ_d for the different specimens, plotted as a function of CaCO_3 content in Figure 13. The slope of $\kappa_d(\text{CaCO}_3)$ was steepest for the lower CaCO_3 contents, decreased as the CaCO_3 content increased, and was essentially zero for the higher values. These results were similar to the correlation between total erosion weight and CaCO_3 content obtained by Jiang & Soga (2017) for sand-gravel mixtures treated with urea- CaCl_2 concentrations ranging between 0.2–2 M. Jiang & Soga however recognised the need for microstructural characterisation to further understand the mechanics behind the improvement of erosion resistance. Figure 13 shows that while for a specific CaCO_3 content, some specimens showed decreasing erodibility values with increasing urea- CaCl_2 solution concentration (*cf.* MICP-0.02 M-10 mm, MICP-0.06 M-15 mm, MICP-0.1 M-25 mm), others showed the opposite (*cf.* MICP-0.06 M-22 mm, MICP-0.08 M). This most likely reflected the changes in the

microstructural fabric, discussed hereafter. It should be noted that the unusual erosion rate increase with CaCO_3 content of specimen MICP-0.08 M is within the bounds of the ICP-OES instrumental error (RSD of $\pm 5\%$); nonetheless it could also be attributed to a decrease in erosion resistance above a critical CaCO_3 crystal size. For instance, Wang (2018) found that CaCO_3 crystal size must be large enough to enhance the unconfined compressive strength performance efficiency (MPa per % CaCO_3) of MICP-treated Fraction D sand, but a further increase may have a negative impact. Thus, a MICP treatment formulation yielding sand particles coated with a film of very small CaCO_3 crystals may be as sub-optimal as one yielding a small quantity of very large crystals. While the former is not expected to contribute towards an enhanced mechanical response, the latter may result in failure through the bulk of uncemented material.

Microstructural fabric characteristics

Microscale parameters of the CaCO_3 crystals precipitated in the fine sand were computed from the reconstructed CT scans. The obtained crystal size data was used to calculate the spatial evolution of crystal size-frequency plots, or crystal size distributions (CSDs) (Kile *et al.*, 2000; Mitchell & Ferris, 2006). For this, group size was set at approximately one fifth of the mean crystal size, considered large enough to mitigate noise (Kile *et al.*, 2000). The mean μ (Equation 16) and variance σ^2 of the natural logarithm of the crystal sizes (Equation 17) were subsequently calculated as follows:

$$\mu = \sum \ln(X) \cdot f(X) \quad (16)$$

$$\sigma^2 = \sum (\ln(X) - \alpha)^2 \cdot f(X) \quad (17)$$

where X is the crystal group size and $f(X)$ is the frequency of crystals for that size.

As evidenced by Figure 14, the shape of the CSDs was dependent on the urea- CaCl_2 solution concentration. An asymptotic CSD, in which the frequency of the sizes are greatest in the smallest size classes, was produced by the 0.02 M solution (Figure 14a). As nucleation decreased and size-dependant growth started to establish, the CSD shape evolved towards a bimodal shape (0.04 and 0.06 M, Figure 14b). Finally, a lognormal CSD, whereby existing crystals grow at the expense of nucleation, developed from the 0.08 and 0.1 M solutions (Figure 14c). This difference in growing mechanism was also discernible from Figure 15, showing that σ^2 increased linearly with μ . Namely, while low urea- CaCl_2 solution concentrations yielded small and relatively uniform crystal sizes, higher concentrations produced a distinctly variable profile. This may be explained by a decaying nucleation rate accompanied by a size dependent growth, during which larger crystals tend to grow faster (this is also known as surface-controlled Law of Proportionate Effect) (Kile *et al.*, 2000). CSD shapes were further corroborated by the SEM BSE images in Figure 14 showing a coupled increase in crystal size and variance with solution molarity.

Following a similar approach to the one adopted to determine the particle size distribution of soils, crystal gradation curves were computed with respect to the cumulative calcite volume, used as the weighing parameter (ASTM D6913/D6913M-17, 2017; Terzis & Laloui, 2018). Results are shown in Figure 16, together with the particle size distribution of untreated Fraction D sand. The average diameter at 50% (D_{50}) was used as an indicator of the size range of the calcite crystals. For example, for specimen MICP-0.02 M, D_{50} ranged between $85 \pm 10 \mu\text{m}$, while for specimen MICP-0.1 M it ranged between $210 \pm 30 \mu\text{m}$. In addition, it is noteworthy that CSDs evolved from uniformly graded ($C_u = 2-3$) to slightly gap graded (

$C_u > 3$)—or having CaCO_3 particles with different size ranges—with increasing urea- CaCl_2 solution concentrations. This difference was also reflected by the higher CSD variances. Specimens MICP-0.02 M, MICP-0.06 M, and MICP-0.1 M are plotted in Figures 14-16 as representative examples, but crystal diameter data for all specimens are summarised in Table 4. By comparing Figure 13 with Figure 16 it is clear that for the same CaCO_3 content, larger crystals led to a lower erodibility. However, results for MICP-0.08 M, corresponding to the largest crystal sizes, may suggest the existence of a threshold crystal diameter, above which the erodibility increases again. Further EFA experiments are nonetheless required to confirm this hypothesis.

Regarding the validity of the results from the XRCT scans, calculated microstructural characteristics for the Fraction D sand of specimen MICP-0.04 M were compared with parameters measured directly under the SEM microscope. For this, SEM images were acquired at six different specimen heights, providing a size range for the precipitated CaCO_3 particles. Following the notation introduced above, specimen MICP-0.04 M-25.1 mm refers to a cross-section 25.1 mm from the coarse-fine sand interface. SEM crystal size data is summarised in Table 5.

CSDs having lognormal and asymptotic shapes were generated from the SEM images for the bottom (MICP-0.04 M-21.5 mm) and the interface (MICP-0.04 M-4.35 mm) of the specimen, respectively. Results are presented for comparison with the XRCT data in Figure 17a. It is clear that distributions generated by both methods were in good agreement, with XRCT data falling within the envelope provided by the SEM results. μ and σ^2 values calculated from the SEM images were as much as four times lower than those based on the XRCT data, implying overall smaller and more disperse crystal sizes (Table 5). This was further evidenced by the particle gradation curves obtained via the two different methods (Figure 17b). While the D_{50} obtained from the SEM images ranged between $12 \pm 9 \mu\text{m}$, XRCT data yielded values ranging between $98 \pm 15 \mu\text{m}$. Furthermore, discrepancies were also found in the shape of the gradation curves themselves, with results obtained from the SEM images failing to capture the distribution of the larger CaCO_3 crystals, thus resulting in “cut”-looking curves for values above approximately D_{80} . Nonetheless, except for the sub-sample closer to the coarse-fine sand interface (MICP-0.04 M-4.35 mm), results obtained for the shape factors C_u and C_c agreed reasonably well and indicated a uniformly graded CaCO_3 distribution.

In addition, calcite contents were numerically calculated from the XRCT data and compared with direct measurements from ICP-OES (Figure 4). Similar to the gradation curves, results revealed a difference of one order of magnitude, with direct and indirect measurements for the fine sand being equal to 0.2-0.8% and 0.03%, respectively. Similarly, ICP-OES measurements for the coarse sand ranged between 0.6-0.8%, while a value of 0.13% was obtained from the XRCT data. The error for the coarse sand was smaller due to the lower frequency of crystals with diameters below $13 \mu\text{m}$.

From these observations it is clear that while measurements obtained from XRCT were adequate for assessing trends, calculated numerical values varied greatly when compared to direct measurements. Some reasons for these differences could include:

- Limitations in the maximum resolution achieved by the XRCT, unable to detect particles below $13 \mu\text{m}$.
- No crystal separation method was used to separate interconnected calcite crystals in the XRCT data, hindering the accurate determination of their numbers and

volumes. This would account for the unusual crystal gradation curve obtained for MICP-0.1 M, with crystal grain sizes larger than those of Fraction D sand.

- Limitation of SEM images to the scale of a few grains.
- Presence of CaCO_3 phases other than calcite, *e.g.* vaterite, with an equivalent density to silica sand (2.65g/cm^3) (Chakoumakos *et al.*, 2016). While their presence could not be captured by XRCT, these would have been included in the SEM and CaCO_3 content analyses.

While the first three were direct consequences of the equipment and methods employed, the possibility of the latter is currently being investigated.

CONCLUSION

Erosion tests of MICP-treated fine sand were conducted using a newly designed EFA and the sample structure was investigated with XRCT. The results showed for the first time how the microstructural distribution of CaCO_3 influences the erodibility of sand specimens, suggesting how MICP treatment can be optimised in this area. Erosion-time series and erosion rates were obtained for specimens treated with urea- CaCl_2 solution concentrations ranging between 0.02-0.1 M. As a result, correlations were drawn between erosion rate, excess shear stress, and microstructural features for MICP-treated fine sand. The major conclusions were:

1. In the context of one-dimensional MICP by gravity flow from the coarse fraction to the fine fraction, the coarse-fine sand configuration caused a “preferential” CaCO_3 precipitation along the interface zone, most likely due to bacterial aggregation in the coarse sand. Capitalising on this phenomenon may be an effective way of localising MICP treatment at the core-filter interfaces of earth embankment dams, and at the gravel pack-formation interface of oil- and gas-producing wells.
2. MICP treatment contributed to a reduction in the cumulative height eroded relative to non-MICP specimens. For the tested fluid flow velocities, duration, and fine sand, a urea- CaCl_2 solution concentration higher than 0.04 M reduced cumulative height eroded by a factor of 10 and concentrations above 0.08 M brought values down to a negligible level.
3. The MICP treatment modified the erosion resistance properties of fine sand. While untreated specimens eroded primarily in particulate and mass form, MICP-treated specimens were characterised by a block erosion mechanism. The formation of these clusters was fundamentally responsible for the observed erosion relaxation behaviour. However, as a consequence, specimens became more brittle, with cracks developing parallel to the direction of the flow.
4. Erodibility was a decreasing function of CaCO_3 content for low urea- CaCl_2 solution concentrations and essentially independent of CaCO_3 content for higher concentrations. For a particular CaCO_3 content and as the urea- CaCl_2 solution concentration increased, the erodibility decreased. Therefore, the effectiveness of MICP for surface erosion control was dominated both by the amount of CaCO_3 precipitated and its microstructural features, with higher CaCO_3 contents and bigger crystals yielding lower erodibility values.
5. Three basic shapes of CaCO_3 CSDs were observed in the fine sand: asymptotic, bimodal, and log-normal, indicating a transition of crystal precipitation process. As a result, crystal mean size and variance increased with urea- CaCl_2 solution concentration. For a given bacterial density and granular material, this opens up the possibility of predicting a particular crystal growth mechanism by applying the appropriate urea- CaCl_2 solution concentrations.

Overall, this study gives a new understanding of the link between MICP parameters, calcite crystal properties, and surface erosion behaviour of MICP-treated sands. This forms a new basis for the conception of erosion models that incorporate notions of microscopic quantities affecting the macro-scale behaviour. While the instrumental techniques and the EFA setup successfully captured the CaCO_3 microstructure and tangential flow-induced surface erosion mechanics, the obtained results remain a singular data set. Additional testing is needed over a greater range of MICP treatment formulations (*i.e.* OD_{600} , urea- CaCl_2 solution concentrations) to expand the database, making a more robust analysis possible.

ACKNOWLEDGEMENTS

The authors would like to thank John Chandler, Kristian Pether, Mark Smith, Chris McGinnie, and Chris Knight for facilitating the EFA experiments; and Len Howlett for his assistance with SEM imaging. The authors would also like to acknowledge the EPSRC Centre for Doctoral Training in Future Infrastructure and Built Environment at the University of Cambridge (EPSRC grant reference number EP/L016095/1).

NOTATION

$D_{10}, D_{30}, D_{50}, D_{60}$	grain sizes; subscript indicates percent smaller
D^*	dimensionless measure of grain size
E	erosion rate
E_c	critical erosion rate (3.6 mm/h)
G	acceleration of gravity (9.81 m/s^2)
k_d, k_d^*	respectively, linear and nonlinear measures of erodibility coefficient
κ_d	erodibility, $\partial E / \partial (\tau - \tau_c)$
m	exponent in erosion law
A, n	regression coefficients used by Roberts et al. (1998)
G_d, G_s	respectively, specific gravities of dry bulk sand and of grains
α	numerical coefficient in dimensionless erosion law used by Walder (2016)
ν	kinematic viscosity of water ($10^{-6} \text{ m}^2/\text{s}$)
ρ_d, ρ_s, ρ_w	respectively, densities of bulk dry sand, grains, and water
$\Phi, \check{\Phi}$	respectively, dimensionless measures of erosion rate used by van Rijn (1984) and Walder (2016)
T	transport stage, $\tau / \tau_c - 1$
τ, τ_c	respectively, shear stress and critical shear stress
C_u	coefficient of uniformity
C_c	coefficient of curvature
μ	natural log crystal mean size
σ^2	crystal size variance
$X, f(X)$	respectively, crystal group size and frequency of crystals for that size
C, k	regression coefficients that depend on the type of sand}
f	friction factor in the Darcy-Weisbach equation
ε	pipe roughness, k_s/D after Nikuradse (1933)
Re	Reynolds number
a, b	respectively, height and width of EFA flume
k_s	grain-related roughness height, $D_{50}/2$
$c[x]$	analyte solution concentration

$M(x)$	molar weight
V_{SOLV}	volume of solvent
w_s	weight of sand

REFERENCES

- Al Qabany, A. & Soga, K. (2013). Effect of chemical treatment used in MICP on engineering properties of cemented soils. *Géotechnique* **63**, No. 4, 331–339, DOI: 10.1680/geot.SIP13.P.022, <http://www.icevirtuallibrary.com/doi/10.1680/geot.SIP13.P.022>
- Amin, M., Zomorodian, S. M.A. & O’Kelly, B. C. (2017). Reducing the hydraulic erosion of sand using microbial-induced carbonate precipitation. *Proceedings of the Institution of Civil Engineers - Ground Improvement* **170**, No. 2, 112–122, DOI: 10.1680/jgrim.16.00028, <http://www.icevirtuallibrary.com/doi/10.1680/jgrim.16.00028>.
- ASTM D6913/D6913M-17 (2017). Standard Test Methods for Particle-Size Distribution (Gradation) of Soils Using Sieve Analysis. DOI: 10.1520/D6913{\-}D6913M-17.
- Béguin, R. (2011). *Etude multi-échelle de l'érosion de contact au sein des ouvrages hydrauliques en terre*. Ph.D. thesis, Université de Grenoble, <https://tel.archives-ouvertes.fr/tel-00680078>.
- Béguin, R., Oxarango, L., Sapin, L., Garandet, A., Viglino, A., François, E., Mora, H., Martins, F., Duchesne, L., Albrecht, D., Esnault-Filet, A., Gutjahr, I. & Lépine, L. (2019). Experimental Tests of Soil Reinforcement Against Erosion and Liquefaction by Microbially Induced Carbonate Precipitation. In *Internal Erosion in Earthdams, Dikes and Levees. EWG-IE 2018. Lecture Notes in Civil Engineering*. (Bonelli, S., Jommi, S. & Sterpi, D., eds.), Springer, Cham, pp. 16–24, doi:10.1007/978-3-319-99423-9{\-}2, URL http://link.springer.com/10.1007/978-3-319-99423-9_2.

Bonelli, S. (2013). *Erosion in Geomechanics Applied to Dams and Levees*. First edit edn.,

Wiley ISTE.

Briaud, Ting, F. C. K., Chen, H. C., Gudavalli, R., Perugu, S. & Wei, G. (1999). SRICOS:

Prediction of Scour Rate in Cohesive Soils at Bridge Piers. *Journal of Geotechnical and Geoenvironmental Engineering* **125**, No. April, 237–246.

Briaud, J. L., Ting, F. C. K., Chen, H. C., Cao, Y., Han, S. W. & Kwak, K. W. (2001).

Erosion Function Apparatus for Scour Rate Predictions. *Journal of Geotechnical and Geoenvironmental Engineering* **127**, No. 2, 105–113, DOI: 10.1061/(ASCE)1090-0241(2001)127:2(105), URL <http://ascelibrary.org/doi/10.1061/%28ASCE%291090-0241%282001%29127%3A2%28105%29>.

Chakoumakos, B. C., Pracheil, B. M., Koenigs, R. P., Bruch, R. M. & Feygenson, M. (2016).

Empirically testing vaterite structural models using neutron diffraction and thermal analysis. *Scientific Reports* **6**, No. 1, 36799, DOI: 10.1038/srep36799, <http://www.nature.com/articles/srep36799>.

Clarà Saracho, A. & Haigh, S. (2018a). Experimental optimization of microbially induced calcite precipitation (MICP) for contact erosion control in earth dams. In *Scour and Erosion IX: Proceedings of the 9th International Conference on Scour and Erosion (ICSE 2018), November 5-8, 2018, Taipei, Taiwan*, Ch. Book chapt, Taipei: CRC Press, pp. 43–50, DOI: 10.17863/CAM.41464.

Clarà Saracho, A. & Haigh, S. (2018b). Microbially Induced Calcite Precipitation (MICP) to mitigate contact erosion in earth dams and levees. In *38th USSD Annual Conference and Exhibition*, United States Society on Dams, DOI: 10.17863/CAM.41847.

Dadda, A., Geindreau, C., Emeriault, F., du Roscoat, S., Esnault Filet, A. & Garandet, A. (2019). Characterization of contact properties in biocemented sand using 3D X-ray

micro-tomography. *Acta Geotechnica* **14**, No. 3, 597–613, DOI: 10.1007/s11440-018-0744-4, <https://doi.org/10.1007/s11440-018-0744-4>.

Damgaard, J. S., Whitehouse, R. J. S. & Soulsby, R. L. (1997). Bed-Load Sediment Transport on Steep Longitudinal Slopes. *Journal of Hydraulic Engineering* **123**, No. 12, 1130–1138, DOI: 10.1061/(ASCE)0733-9429(1997)123:12(1130), URL <http://ascelibrary.org/doi/10.1061/%28ASCE%290733-9429%281997%29123%3A12%281130%29>

Gao, Y., Tang, X., Chu, J. & He, J. (2019). Microbially Induced Calcite Precipitation for Seepage Control in Sandy Soil. *Geomicrobiology Journal* **36**, No. 4, 366–375, DOI: 10.1080/01490451.2018.1556750, URL <https://doi.org/10.1080/01490451.2018.1556750>.

Hammes, F., Boon, N., de Villiers, J., Verstraete, W. & Siciliano, S. D. (2003). Strain-Specific Ureolytic Microbial Calcium Carbonate Precipitation. *Applied and Environmental Microbiology* **69**, No. 8, 4901–4909, DOI: 10.1128/AEM.69.8.4901-4909.2003, <http://aem.asm.org/cgi/doi/10.1128/AEM.69.8.4901-4909.2003>.

Haouzi, F. Z., Esnault-Filet, A. & Courcelles, B. (2020). Optimization of Microbially Induced Calcite Precipitation (MICP) Protocol Against Erosion. *Environmental Geotechnics*, 1–10 DOI: 10.1680/jenge.19.00083, <https://www.icevirtuallibrary.com/doi/10.1680/jenge.19.00083>.

ICOLD (2016). Internal erosion of existing dams, levees and dikes, and their foundations: Case histories, investigations, testing, remediation and surveillance. *Technical Report February*, International Commission on Large Dams.

Jiang, N. & Soga, K. (2017). The applicability of microbially induced calcite precipitation (MICP) for internal erosion control in gravel-sand mixtures. *Géotechnique* **67**, No. 1,

42–55, DOI: 10.1680/jgeot.15.P.182,

<http://www.icevirtuallibrary.com/doi/10.1680/jgeot.15.P.182>.

- Jiang, N.-J., Soga, K. & Kuo, M. (2017). Microbially Induced Carbonate Precipitation (MICP) for Seepage-Induced Internal Erosion Control in Sand-Clay Mixtures. *Journal of Geotechnical and Geoenvironmental Engineering* **143**, 4016100, DOI: 10.1061/(ASCE)GT.1943-5606.0001559.
- Jiang, N.-J., Soga, K. & Yamamoto, K. (2018). A High-Pressure Plane-Strain Testing System to Evaluate Microbially Induced Calcite Precipitation as a Sand Production Control Method. In *Proceedings of GeoShanghai 2018 International Conference: Geoenvironment and Geohazard*, Singapore: Springer Singapore, pp. 499–506, doi:10.1007/978-981-13-0128-5_{-}55, URL http://link.springer.com/10.1007/978-981-13-0128-5_55.
- Jiang, N.-J., Tang, C.-S., Yin, L.-y., Xie, Y.-H. & Shi, B. (2019). Applicability of Microbial Calcification Method for Sandy-Slope Surface Erosion Control. *Journal of Materials in Civil Engineering* **31**, 4019250, DOI: 10.1061/(ASCE)MT.1943-5533.0002897.
- Kile, D., Eberl, D., Hoch, A. & Reddy, M. (2000). An assessment of calcite crystal growth mechanisms based on crystal size distributions. *Geochimica et Cosmochimica Acta* **64**, No. 17, 2937–2950, DOI: 10.1016/S0016-7037(00)00394-X, <https://linkinghub.elsevier.com/retrieve/pii/S001670370000394X>.
- Mahmood, M. N., Sultan, Z. & Yousuf, N. (2018). Scenario of Sand Production from Hydrocarbon Reservoir And Its Mitigation. *Journal of Recent Activities in Production* **3**, No. 1.
- McNeil, J., Taylor, C. & Lick, W. (1996). Measurements of Erosion of Undisturbed Bottom Sediments with Depth. *Journal of Hydraulic Engineering* **122**, No. 6, 316–324, DOI:

10.1061/(ASCE)0733-9429(1996)122:6(316),

<http://ascelibrary.org/doi/10.1061%28ASCE%290733->

[9429%281996%29122%3A6%28316%29](http://ascelibrary.org/doi/10.1061%28ASCE%290733-9429%281996%29122%3A6%28316%29).

Mitchell, A. C. & Ferris, F. G. (2006). The Influence of *Bacillus pasteurii* on the Nucleation and Growth of Calcium Carbonate. *Geomicrobiology Journal* **23**, No. 3-4, 213–226,

DOI: 10.1080/01490450600724233,

<https://www.tandfonline.com/doi/full/10.1080/01490450600724233>.

Moody, L. F. (1944). Friction factors for pipe flow. *Trans. ASME* **66**, No. 671.

Murphy, A. (2018). *Sediment Heterogeneity and Sand Production in Gas Hydrate*

Extraction: Daini-Atsumi Knoll, Nankai Trough, Japan. Ph.D. thesis, University of

Cambridge, DOI: 10.17863/CAM.30993.

Nikuradse, J. (1933). Tech. Rep. NACA Technical Memorandum 1292. *Stromungsgesetz in*

rauhren rohren, vDI Forschungshefte 361 (English translation: Laws of flow in rough pipes).

Philippe, P., Beguin, R. & Faure, Y.-H. (2013). Contact Erosion. In *Erosion in Geomechanics*

Applied to Dams and Levees (Bonelli, S. & Nicot, F., eds.), Ch. 2, Hoboken, NJ,

USA: John Wiley & Sons, Inc., pp. 101–191, DOI: 10.1002/9781118577165.ch2,

<http://doi.wiley.com/10.1002/9781118577165.ch2>.

Ravens, T. M. & Gschwend, P. M. (1999). Flume Measurements of Sediment Erodibility in

Boston Harbor. *Journal of Hydraulic Engineering* **125**, No. 10, 998–1005, DOI:

10.1061/(ASCE)0733-9429(1999)125:10(998), URL

<http://ascelibrary.org/doi/10.1061/%28ASCE%290733->

[9429%281999%29125%3A10%28998%29](http://ascelibrary.org/doi/10.1061/%28ASCE%290733-9429%281999%29125%3A10%28998%29).

Reddi, L., Lee, I.-M. & Bonala, M. (2000). Comparison of Internal and Surface Erosion

Using Flow Pump Tests on a Sand-Kaolinite Mixture. *Geotechnical Testing Journal*

23, No. 1, 116, DOI: 10.1520/GTJ11129J,

<http://www.astm.org/doiLink.cgi?GTJ11129J>.

Regazzoni, P.-L. & Marot, D. (2013). A comparative analysis of interface erosion tests.

Natural Hazards **67**, No. 2, 937–950, DOI: 10.1007/s11069-013-0620-3,

<http://link.springer.com/10.1007/s11069-013-0620-3>.

Roberts, J., Jepsen, R., Gotthard, D. & Lick, W. (1998). Effects of Particle Size and Bulk

Density on Erosion of Quartz Particles. *Journal of Hydraulic Engineering* **124**, No.

12, 1261–1267, DOI: 10.1061/(ASCE)0733-9429(1998)124:12(1261),

[http://ascelibrary.org/doi/10.1061/%28ASCE%290733-](http://ascelibrary.org/doi/10.1061/%28ASCE%290733-9429%281998%29124%3A12%281261%29)

[9429%281998%29124%3A12%281261%29](http://ascelibrary.org/doi/10.1061/%28ASCE%290733-9429%281998%29124%3A12%281261%29).

Rodriguez-Navarro, C., Jimenez-Lopez, C., Rodriguez-Navarro, A., Gonzalez-Muñoz, M. T.

& Rodriguez-Gallego, M. (2007). Bacterially mediated mineralization of vaterite.

Geochimica et Cosmochimica Acta **71**, No. 5, 1197–1213, DOI:

10.1016/j.gca.2006.11.031,

<http://linkinghub.elsevier.com/retrieve/pii/S0016703706022186>.

Salifu, E., MacLachlan, E., Iyer, K. R., Knapp, C. W. & Tarantino, A. (2016). Application of

microbially induced calcite precipitation in erosion mitigation and stabilisation of

sandy soil foreshore slopes: A preliminary investigation. *Engineering Geology* **201**,

96–105, DOI: 10.1016/j.enggeo.2015.12.027, URL

<https://linkinghub.elsevier.com/retrieve/pii/S0013795215301228>.

Shields, A. (1936). Anwendung der Aehnlichkeits-Mechanik und der Turnulenzforschung auf

die Geschiebebewegung. *Preussische Versuchsanstalt fur Wasserbau and Schiffbau* .

Suzuki, K., Schultheiss, P., Nakatsuka, Y., Ito, T., Egawa, K., Holland, M. & Yamamoto, K.

(2015). Physical properties and sedimentological features of hydrate-bearing samples recovered from the first gas hydrate production test site on Daini-Atsumi Knoll around eastern Nankai Trough. *Marine and Petroleum Geology* **66**, 346–357, DOI: 10.1016/j.marpetgeo.2015.02.025, URL <https://linkinghub.elsevier.com/retrieve/pii/S0264817215000574>.

Terzaghi, K. (1922). Der Grundbruch an Stauwerken und Seine Verhütung. *Verhütung Forcheimer-Nummer Wasserkr* **17**, No. 24, 445–449.

Terzis, D. & Laloui, L. (2018). 3-D micro-architecture and mechanical response of soil cemented via microbial-induced calcite precipitation. *Scientific Reports* **8**, No. 1, 1416, DOI: 10.1038/s41598-018-19895-w, URL <http://www.nature.com/articles/s41598-018-19895-w>.

van Rijn, L. C. (1984). Sediment Pick-Up Functions. *Journal of Hydraulic Engineering* **110**, No. 10, 1494–1502, DOI: 10.1061/(ASCE)0733-9429(1984)110:10(1494), See <http://ascelibrary.org/doi/10.1061/%28ASCE%290733-9429%281984%29110%3A10%281494%29>.

Walder, J. S. (2016). Dimensionless Erosion Laws for Cohesive Sediment. *Journal of Hydraulic Engineering* **142**, No. 2, 04015047, DOI: 10.1061/(ASCE)HY.1943-7900.0001068, URL <http://ascelibrary.org/doi/10.1061/%28ASCE%29HY.1943-7900.0001068>

Wang, X., Tao, J., Bao, R., Tran, T. & Tucker-Kulesza, S. (2018). Surficial Soil Stabilization against Water-Induced Erosion Using Polymer-Modified Microbially Induced Carbonate Precipitation. *Journal of Materials in Civil Engineering* **30**, No. 10,

Accepted manuscript doi: 10.1680/jgeot.19.p.350

04018267, DOI: 10.1061/(ASCE)MT.1943-5533.0002490, URL

<http://ascelibrary.org/doi/10.1061/%28ASCE%29MT.1943-5533.0002490>

Wang, Y. (2018). *Microbial-Induced Calcium Carbonate Precipitation: from micro to macro scale*. Ph.D. thesis, University of Cambridge.

Whiffin, V. S. (2004). *Microbial CaCO₃ Precipitation for the Production of Biocement*.

Ph.D. thesis, Murdoch University, Western Australia, DOI:

<http://researchrepository.murdoch.edu.au/399/2/02Whole.pdf>.

Whiffin, V. S., Van Paassen, L. A. & Harkes, M. P. (2007). Microbial Carbonate Precipitation as a Soil Improvement Technique. *Geomicrobiology Journal* **24**, No. January, 417–423, DOI: 10.1080/01490450701436505.

White, S. J. (1970). Plane Bed Thresholds of Fine Grained Sediments. *Nature* **228**, No. 5267, 152–153, DOI: 10.1038/228152a0, <http://www.nature.com/articles/228152a0>.

Winterwerp, J. C., van Kesteren, W. G. M., van Prooijen, B. & Jacobs, W. (2012). A conceptual framework for shear flow–induced erosion of soft cohesive sediment beds. *Journal of Geophysical Research: Oceans* **117**, No. C10, DOI: 10.1029/2012JC008072, URL

<https://agupubs.onlinelibrary.wiley.com/doi/abs/10.1029/2012JC008072>.

Yamamoto, K., Kanno, T., Wang, X.-X., Tamaki, M., Fujii, T., Chee, S.-S., Wang, X.-W.,

Pimenov, V. & Shako, V. (2017). Thermal responses of a gas hydrate-bearing sediment to a depressurization operation. *RSC Advances* **7**, No. 10, 5554–5577, DOI:

10.1039/C6RA26487E, URL <http://dx.doi.org/10.1039/C6RA26487E>.

Table 1. Untreated specimen properties.

Untreated sand properties	Fraction D sand
Specific gravity, G_s	2.65
D_{10} (mm)	0.165
D_{50} (mm)	0.210
Maximum void ratio, e_{max}	0.988
Minimum void ratio, e_{min}	0.585
Silicon dioxide (%)	>98
Dry bulk density, ρ_d (g/cm ³)	1.65
Void ratio, e	0.61
Specimen dimensions	
Height (mm)	50
Diameter (mm)	32.13

Table 2. Cementation treatment formulations.

Specimen name ^a	CaCl ₂ (M) ^b	Urea (M) ^b	Nutrient broth (g L ⁻¹)	NaHCO ₃ (g L ⁻¹)	Number of injections	Injection point	Reaction time (h)
MICP-0.02 M	0.02	0.03	3	10	10	Top	24
MICP-0.04 M	0.04	0.06					
MICP-0.06 M	0.06	0.09					
MICP-0.08 M	0.08	0.12					
MICP-0.1 M	0.1	0.15					

a Names describe total concentration of CaCl₂.

b Whole ratio of urea to CaCl₂ concentration of 3:2.

Table 3. Summary statistics for ICP-OES calibration.

c[Ca ²⁺] (mgL ⁻¹)	Mean intensity		RSD	Accuracy
	Measured	Back-calc.	(%)	(%)
1.0	33.8	58.2	40.6	58.1
10.0	608.8	582.4	1.9	104.5
40.0	2471.2	2329.7	0.7	106.1
80.0	4755.3	4659.4	0.7	102.1
100.0	5866.9	5824.2	0.9	100.7
150.0	8617.3	8736.3	0.7	98.6

Table 4. Summary of crystal size data (μm) for calcite crystals induced by increasing urea- CaCl_2 solution concentrations in Fraction D sand.

	MICP-0.02 M	MICP-0.04 M	MICP-0.06 M	MICP-0.08 M	MICP-0.1 M
Mean	57	61	62	94	83
D_{10}	51	55	55	147	85
D_{30}	71	79	76	164	138
D_{50}	85 ± 10	100 ± 12	96 ± 14	240 ± 40	210 ± 30
D_{60}	90	101	106	308	268
Coefficient of uniformity, C_u	1.76	1.82	1.94	3.21	3.15
Coefficient of curvature, C_c	1.08	1.12	0.99	0.75	0.83
Natural Log mean size, μ	3.9	4.0	4.0	4.4	4.2
Size variance, σ^2	0.25	0.27	0.24	0.39	0.36

Table 5. Summary of crystal size data (μm) obtained from SEM images of Fraction D sand of specimen MICP-0.04 M.

MICP-0.04 M						
Distance from coarse-fine sand interface	25.1 mm	21.5 mm	20.8 mm	20.0 mm	11.3 mm	4.35 mm
No. crystals measured	190	190	241	419	150	158
Mean	3.2	2.5	3.6	3.0	3.8	4.1
D_{10}	1.2	2.9	3.5	3.3	4.0	5.6
D_{30}	2.5	4.3	5.1	6.0	6.9	15.6
D_{50}	3.5	5.5	6.7	7.9	9.4	21.2
D_{60}	4.0	6.5	7.6	8.6	11.4	25.0
Coeff. of uniformity, C_u	3.4	2.2	2.2	2.6	2.9	4.5
Coeff. of curvature, C_c	1.3	1.0	1.0	1.2	1.1	1.8
Natural Log mean size, μ	0.88	0.59	0.99	0.65	0.93	0.82
Size variance, σ^2	0.64	0.79	0.75	0.97	0.89	1.02

Figure captions

Figure 1. EFA experimental setup.

Figure 2. Preparation setup of MICP-treated specimens.

Figure 3. Relative standard deviation (RSD), *i.e.* coefficient of variation, of ICP-OES measurements as a function of Ca^{2+} ion concentration and specimen height (negative: fine sand; positive: coarse sand).

Figure 4. CaCO_3 content for MICP-treated specimens as a function of specimen height and urea- CaCl_2 solution concentration.

Figure 5. 3D volume reconstructions and 2D cross-sections obtained from the XRCT scans of specimens MICP-0.02 M, MICP-0.06 M, and MICP-0.1 M.

Figure 6. Cumulative height eroded-time series and schematisation of the transition between erosion modes for the untreated Fraction D sand ($\tau_c = 0.091$ Pa).

Figure 7. Comparison of critical shear stresses calculated for the untreated Fraction D sand with flume tests by Roberts *et al.* (1998) and White (1970) for cohesionless soils. Dotted circle refers to measurements made using crushed plastic.

Figure 8. Cumulative height eroded-time series for MICP-treated Fraction D sand with increasing urea- CaCl_2 solution concentrations: (a) 0.02 M; (b) 0.04 M; (c) 0.06 M; (d) 0.08 M; (e) 0.1 M. The values in mm refer to the starting EFA test distance from the coarse-fine sand interface.

Figure 9. Photographs of MICP-treated cores during and after EFA testing: (a) agglomerate of cemented particles for MICP-0.04 M-15 mm; (b) failure parallel to the direction of the flow for MICP-0.06 M-18 mm; and (c) ultimate fracture in the coarse fraction.

Figure 10. Erosion rate vs. shear stress for untreated Fraction D sand.

Figure 11. Shields diagram showing $\Theta_c = f(D_*)$ and values for Fraction D sand (after Shields 1936).

Figure 12. Erosion rate vs. excess shear stress for MICP-treated Fraction D sand with increasing urea-CaCl₂ solution concentrations: (a) 0.02 M; (b) 0.04 M; (c) 0.06 M; (d) 0.08 M; (e) 0.1 M. The values in mm refer to the starting EFA test distance from the coarse-fine sand interface.

Figure 13. Erodibility κ_d vs. CaCO₃ content for MICP-treated Fraction D sand treated with increasing urea-CaCl₂ solution concentrations. The values in mm refer to the starting EFA test distance from the coarse-fine sand interface.

Figure 14. Comparison of crystal size distributions (CSDs) generated in the Fraction D sand by various urea-CaCl₂ solution concentrations and corresponding SEM BSE images: (a) asymptotic CSD for specimen MICP-0.02 M; (b) bimodal CSD for specimen MICP-0.06 M; and (c) lognormal CSD for specimen MICP-0.1 M.

Figure 15. Size variance (σ^2) vs. natural logarithm of mean crystal size (μ) for calcite crystals precipitated in Fraction D sand by increasing urea-CaCl₂ solution concentrations.

Figure 16. Crystal gradation curves covering the range between minimum and maximum diameter of calcite precipitated in Fraction D sand under increasing urea-CaCl₂ solution molarity.

Figure 17. Comparison of (a) crystal size distributions (CSDs) and (b) crystal gradation curves computed from SEM images and XRCT scans of Fraction D sand in specimen MICP-0.04 M. The values in mm refer to the starting EFA test distance from the coarse-fine sand interface.

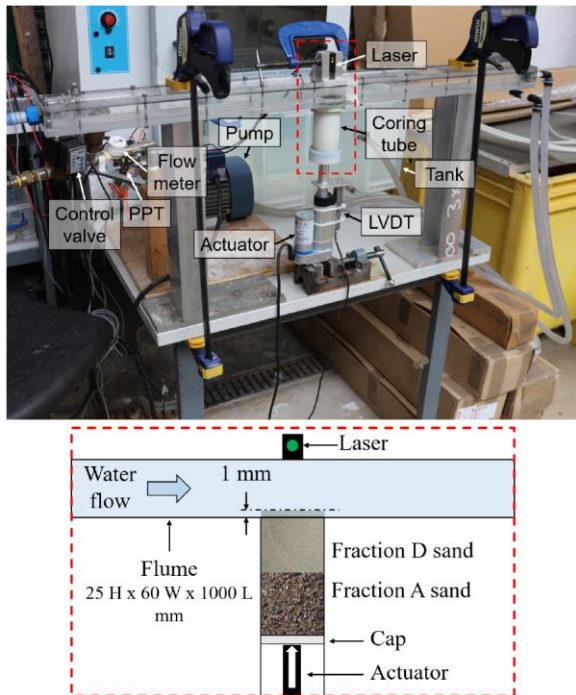


Fig. 1

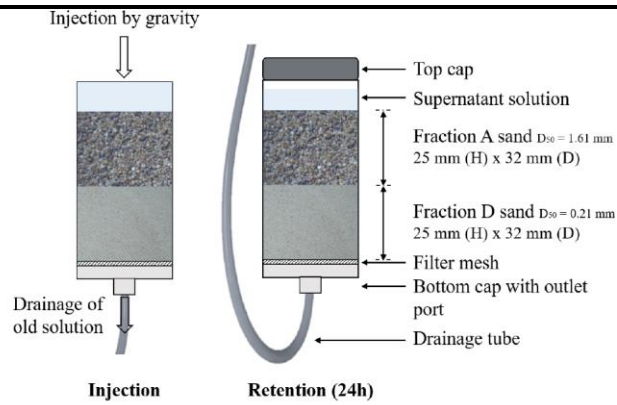


Fig. 2

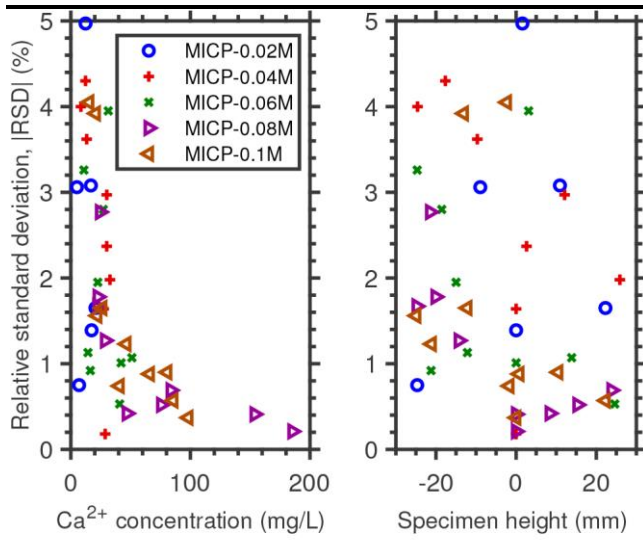


Fig. 3

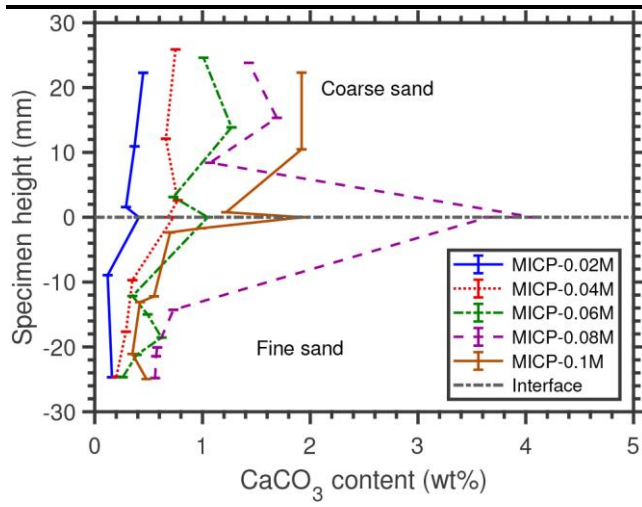


Fig. 4

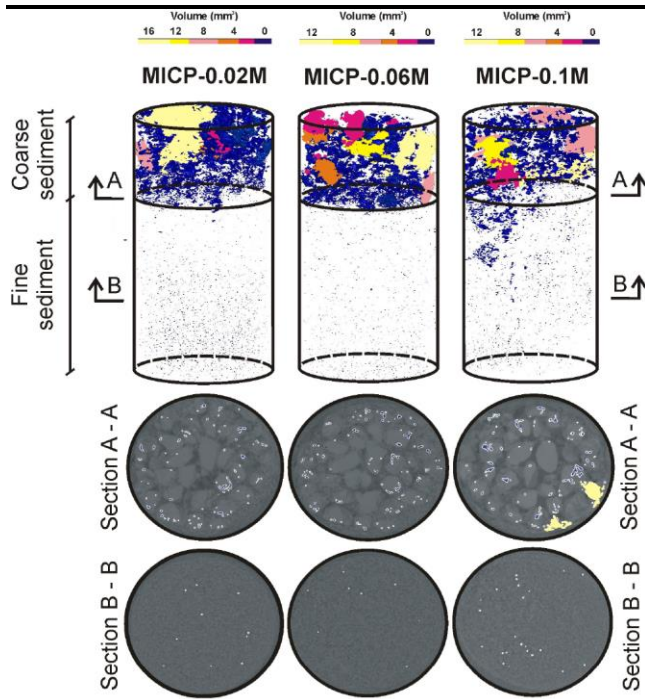


Fig. 5

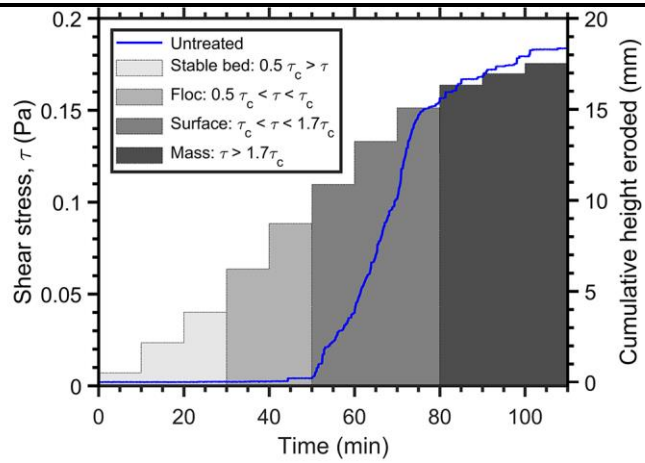


Fig. 6

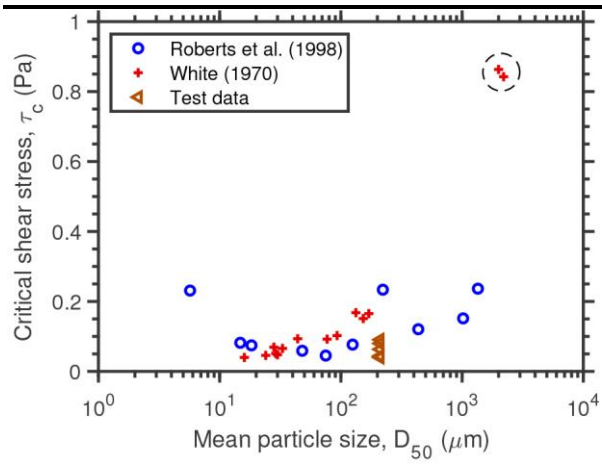


Fig. 7

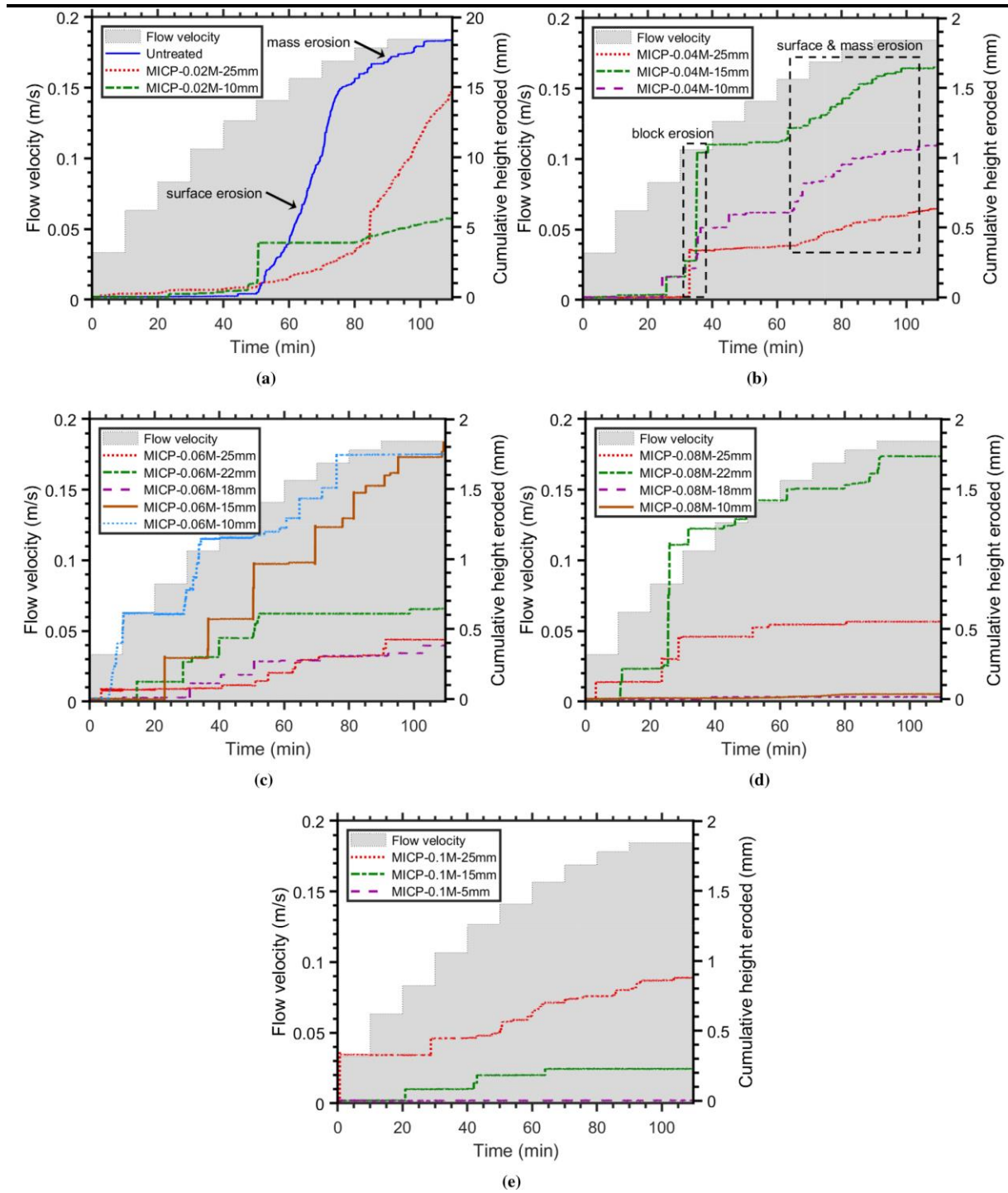


Fig. 8

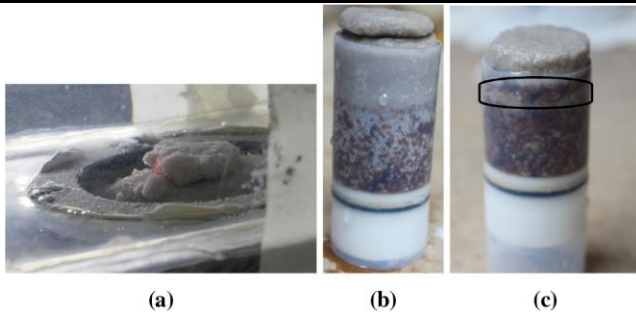


Fig. 9

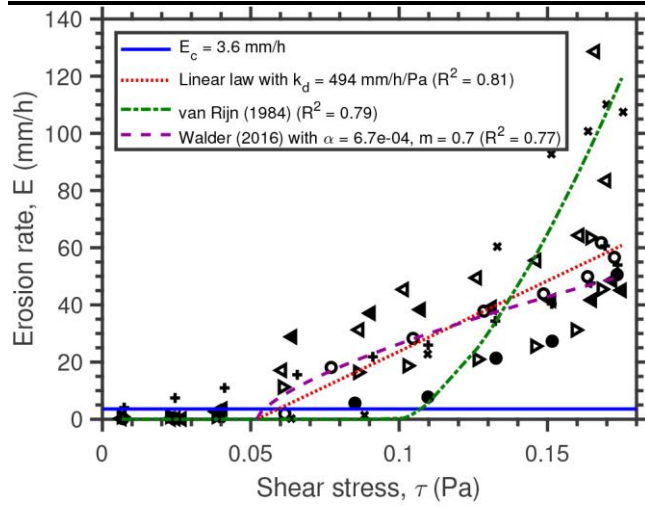


Fig. 10

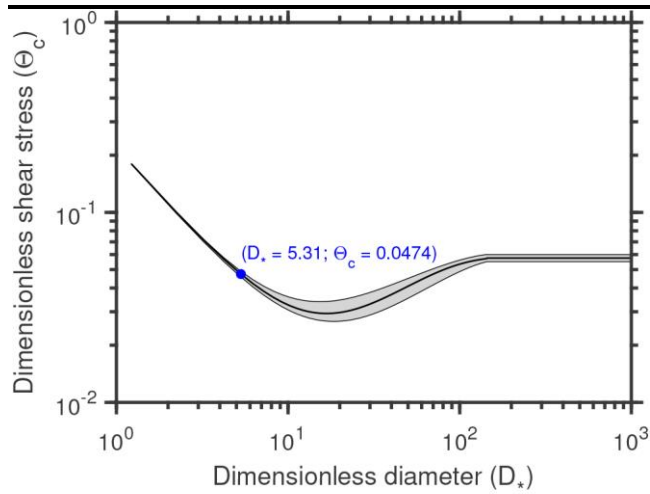


Fig. 11

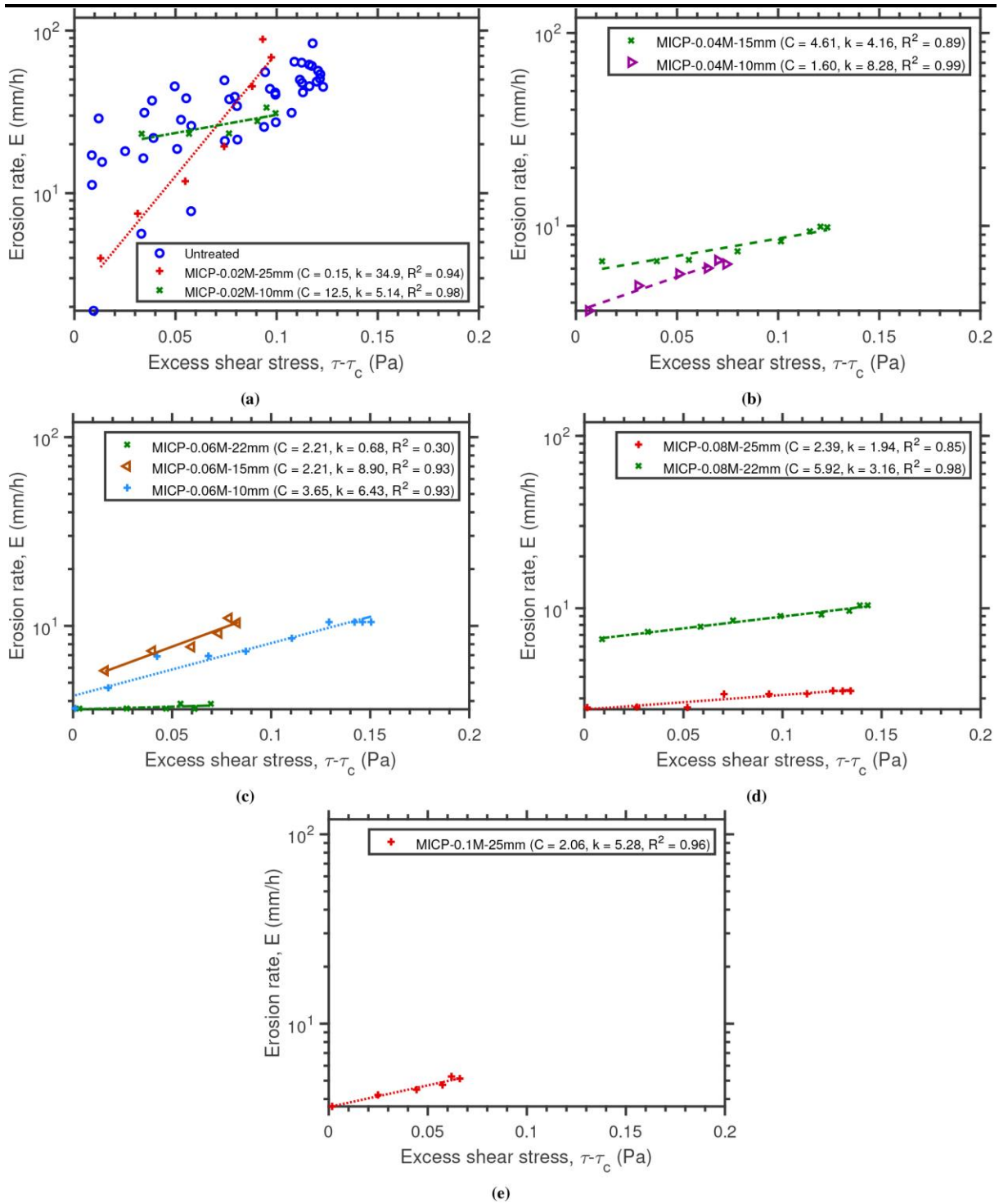


Fig. 12

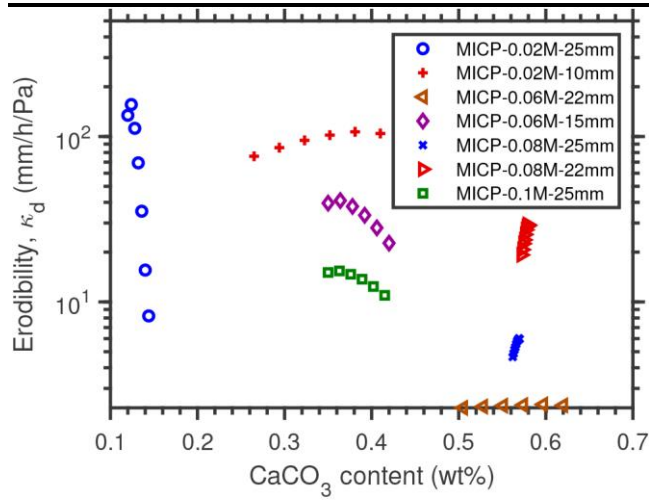


Fig. 13

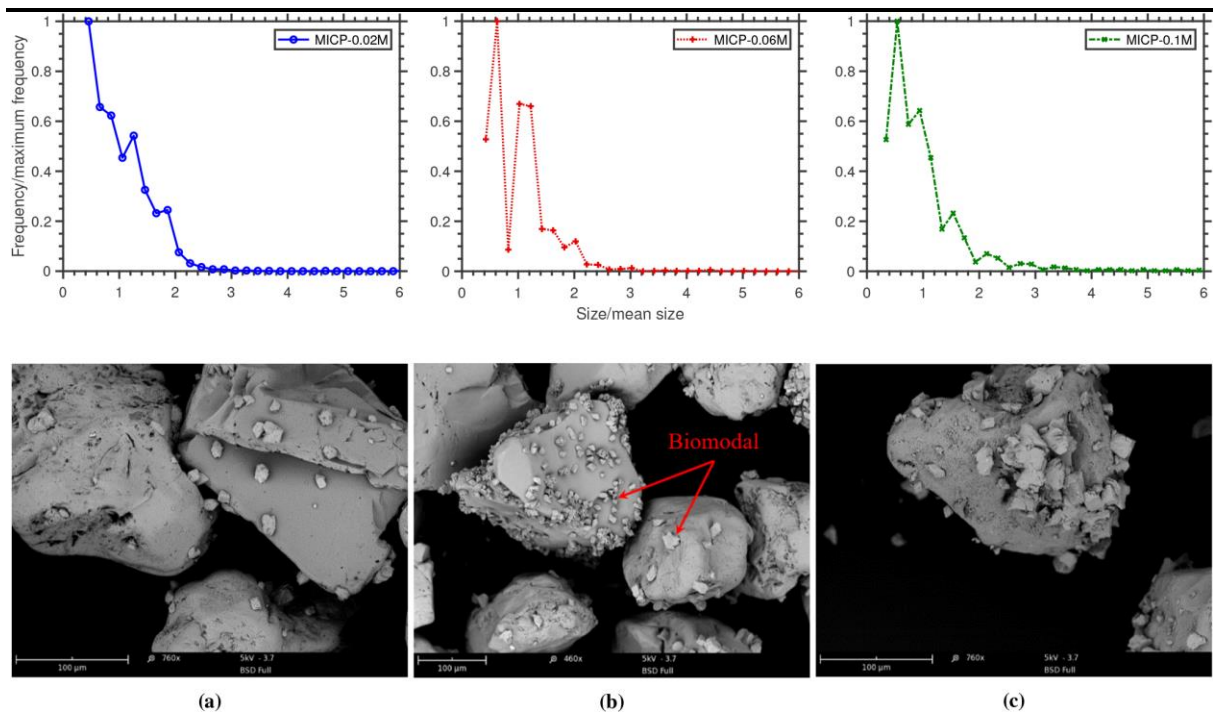


Fig. 14

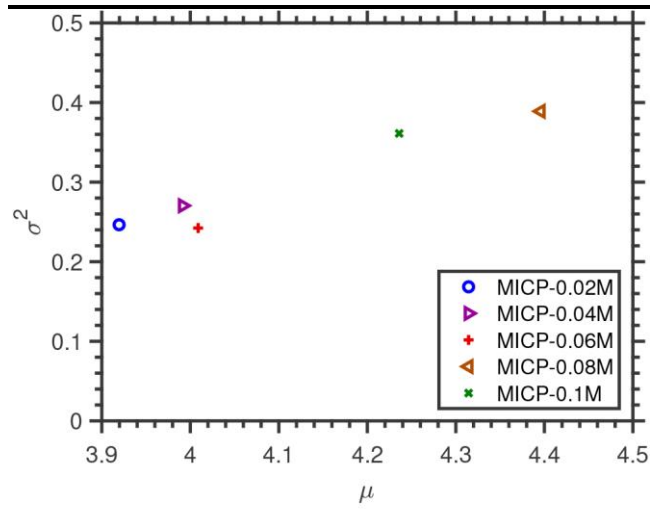


Fig. 15

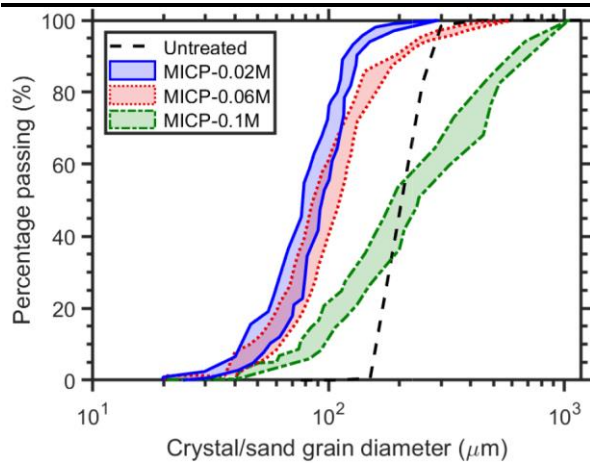
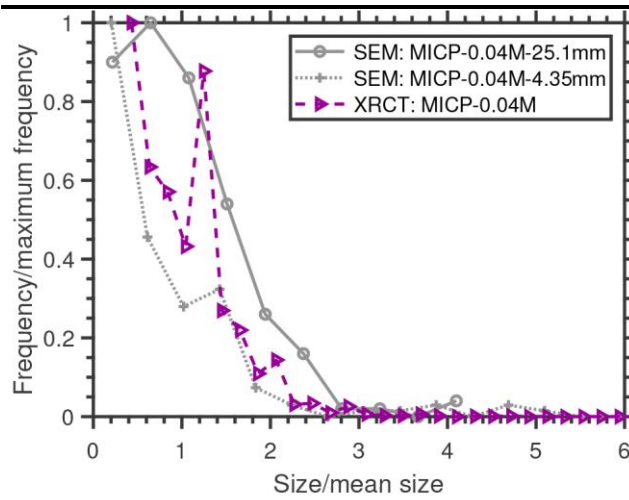
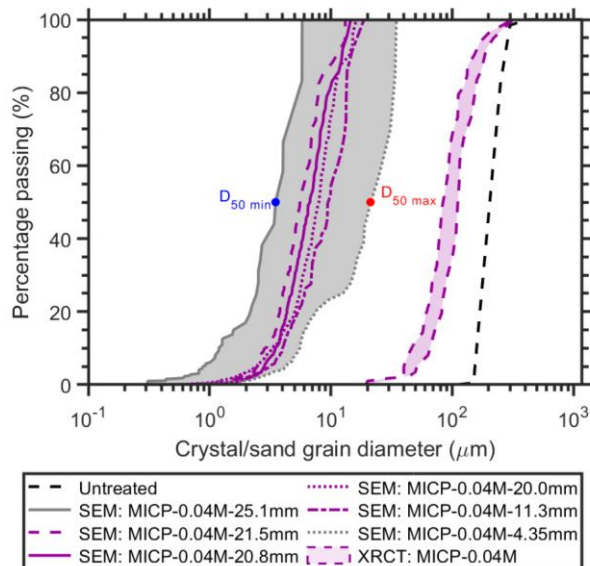


Fig. 16



(a)



(b)

Fig. 17